



**HAL**  
open science

## Ligand-induced incompatible curvatures control ultrathin nanoplatelet polymorphism and chirality

Debora Monego, Sarit Dutta, Doron Grossman, Marion Krapez, Pierre Bauer, Austin Hubley, Jérémie Margueritat, Benoit Mahler, Asaph Widmer-Cooper, Benjamin Abécassis

► **To cite this version:**

Debora Monego, Sarit Dutta, Doron Grossman, Marion Krapez, Pierre Bauer, et al.. Ligand-induced incompatible curvatures control ultrathin nanoplatelet polymorphism and chirality. Proceedings of the National Academy of Sciences of the United States of America, 2024, 121 (9), pp.e2316299121. 10.1073/pnas.2316299121 . hal-04562464

**HAL Id: hal-04562464**

**<https://hal.science/hal-04562464v1>**

Submitted on 15 Oct 2024

**HAL** is a multi-disciplinary open access archive for the deposit and dissemination of scientific research documents, whether they are published or not. The documents may come from teaching and research institutions in France or abroad, or from public or private research centers.

L'archive ouverte pluridisciplinaire **HAL**, est destinée au dépôt et à la diffusion de documents scientifiques de niveau recherche, publiés ou non, émanant des établissements d'enseignement et de recherche français ou étrangers, des laboratoires publics ou privés.

# Ligand-induced incompatible curvatures control ultrathin nanoplatelet polymorphism and chirality

Debora Monego,<sup>1,2,\*</sup> Sarit Dutta,<sup>3,\*</sup> Doron Grossman,<sup>4</sup> Marion Krapez,<sup>1,2</sup> Pierre Bauer,<sup>5</sup> Austin Hubley,<sup>3</sup> Jérémie Margueritat,<sup>5</sup> Benoit Mahler,<sup>5</sup> Asaph Widmer-Cooper,<sup>1,2</sup> and Benjamin Abécassis<sup>3</sup>

<sup>1</sup>*ARC Centre of Excellence in Exciton Science, School of Chemistry,  
University of Sydney, Sydney, New South Wales 2006, Australia*

<sup>2</sup>*The University of Sydney Nano Institute, University of Sydney, Sydney, New South Wales 2006, Australia*

<sup>3</sup>*Univ. Lyon, ENS de Lyon, CNRS, Laboratoire de Chimie, F-69342, Lyon, France*

<sup>4</sup>*LadHyX, CNRS, Ecole polytechnique, Institut Polytechnique de Paris, 91128 Palaiseau Cedex, France*

<sup>5</sup>*Univ Lyon, Université Claude Bernard Lyon 1, CNRS,  
Institut Lumière Matière, F-69622, Villeurbanne, France*

(Dated: December 21, 2023)

The ability of thin materials to shape-shift is a common occurrence that leads to dynamic pattern formation and function in natural and man-made structures. However, harnessing this concept to rationally design inorganic structures at the nanoscale has remained far from reach due to a lack of fundamental understanding of the essential physical components. Here, we show that the interaction between organic ligands and the nanocrystal surface is responsible for the full range of chiral shapes seen in colloidal nanoplatelets. The adsorption of ligands results in incompatible curvatures on the top and bottom surfaces of the NPL, causing them to deform into helicoids, helical ribbons, or tubes depending on the lateral dimensions and crystallographic orientation of the NPL. We demonstrate that nanoplatelets belong to the broad class of geometrically frustrated assemblies and exhibit one of their hallmark features: a transition between helicoids and helical ribbons at a critical width. The effective curvature  $\bar{\kappa}$  is the single aggregate parameter that encodes the details of the ligand/surface interaction, determining the nanoplatelets' geometry for a given width and crystallographic orientation. The conceptual framework described here will aid the rational design of dynamic, chiral nanostructures with high fundamental and practical relevance.

Keywords: Nanoplatelet — chirality — polymorphism — incompatible curvatures — helices

Helical structures are fascinating chiral motifs that are found at different length scales in Nature. Ranging from the molecular scale of DNA and proteins to large-scale structures like tornadoes or galaxies, helices can be stabilised by a broad range of driving forces. Beyond their aesthetic appeal, they can impart useful properties, which has inspired the design of novel chiral materials with specific mechanical or optoelectronic characteristics. At the nanometre scale, helical shapes are especially coveted [1] as their chirality can endow them with desirable properties including chirality-induced spin selectivity, circularly polarized luminescence or circular dichroism. In this realm, nanoplatelets (NPL), a class of ultrathin 2D nanoparticles coated with a monolayer of surfactants [2], are particularly relevant because they display both outstanding optical properties and can be deformed into helical shapes and assemblies. Aside from flat and tubular shapes, two kinds of helices have been observed in NPL: purely twisted helicoids with non-zero gaussian curvature and a straight centerline and helical ribbons which have a cylindrical curvature and a helical centerline [3]. The underlying physical mechanism which gives rise to the emergence of this polymorphism is still unknown. It is clear from previous work that ligands play a significant role in controlling NPL shape, since ligand

exchange can induce large shape variations in CdSe and CdTe NPL [4–7]. However, the interplay between the NPL width, thickness, pitch, radius of curvature, crystallographic structure/orientation, and the molecular interactions at and near the ligand/crystal interface needs further rationalization for predictive design to be possible. It is not yet clear which of these parameters are most relevant for shape selection and hence which knob one has to turn to achieve the desired structure. Moreover, the relevant parameters which trigger the transitions between these different shapes have not been identified, which calls for a unifying conceptual framework that can rationalize the complete design space.

We provide here such a framework that comprehensively explains the polymorphism of NPL and the emergence of chirality in these systems. The coexistence of tubes, helicoids and helical ribbons in NPLs leads us to hypothesize that they belong to geometrically frustrated systems in which the bending and stretching energies compete to dictate the shape of thin ribbons along with geometrical constraints. Diverse systems at different length scales, such as surfactants or chiral seed pods obey such a formalism [8–11], with the common physical ingredients being a spontaneous curvature of microscopic origin and a slender geometry. Using extensive molecular dynamics simulations, along with theory and experiments, we show that the spontaneous curvature comes from interaction between the ligands and the NPL crystal surface, which induces directionally anisotropic stresses

\* These authors contributed equally to this work.

on the top and bottom surfaces and, hence, preferred curvature along different crystallographic axes. Chirality results from the angle between the edge of the NPL and the directions of preferred curvature, while the NPL’s specific shape is dictated by the scaling of the bending and stretching energies with respect to its width and thickness.

## POLYMORPHISM OF CDSE NANOPLATELETS

We focus on zinc blende CdSe NPL [14] coated, in their native state by carboxylate groups. NPL can display different geometries depending on their lateral dimensions, thickness, and surface functionality, as illustrated in Figure 1. NPL with lateral dimensions from 5 nm to 15 nm can either be flat or display a twisted helicoidal shape with a non-zero Gaussian curvature in which the centreline corresponds to the [100] crystallographic axis. Tube-like geometries with a mean radius of curvature from 10 nm to 20 nm are observed when the NPLs have a larger lateral dimension (hundreds of nanometers). Several reports show tubular NPL with principal curvatures along either the [110] or  $[1\bar{1}0]$  axes [13, 15, 16]. Finally, helical ribbons have been reported [12, 17]. In this geometry, the Gaussian curvature is also zero, but the centreline is a helix that rotates along the [110] axis with a defined pitch (e.g.,  $p = 25$  nm [17] and  $p = 122$  nm [12]). This geometry is observed for intermediate widths ( $w = 27$  nm [12]) when one of the lateral dimensions is much longer than the other. We thus observe a variety of shapes (helicoid, helical ribbons, and tubes) which depend on the NPL’s width and the crystal lattice’s orientation with respect to the edges. Furthermore, several reports provide evidence of shape changes when the surface chemistry of the NPL is modified *via* ligand exchange [5–7, 13, 15]. This leads us to hypothesize that the interaction between the surface of the NPL and the organic ligands is critical in determining the shape of the NPL.

## LIGAND INDUCED INCOMPATIBLE CURVATURES

To better understand the key ingredients of the ligand / NPL system, we performed an extensive set of molecular dynamics (MD) simulations. We considered zinc-blende CdSe NPL whose top and bottom facets are cadmium rich (001) crystallographic planes coated with acetate and/or oleate ligands (see Methods and SI for details). Along its thickness, an N monolayer (ML) NPL presents N+1 cadmium planes and N selenium planes, corresponding to a thickness  $t$  between 0.6 nm (for 2ML) and 3.5 nm (for 11ML). We first simulated square 3ML CdSe NPL ( $t = 1.1$  nm,  $L = 10$  nm) with sufficient acetate ligands to provide charge neutrality (3.7 ligands/nm<sup>2</sup>, close to the experimentally measured surface density of 4.8 ligands/nm<sup>2</sup>) [18]. Ligands are first adsorbed on the

flat NPL surface while the crystalline configuration of the NPL remains fixed. Figure 2c shows a resulting configuration of ligands on the top and bottom surfaces of the NPL before (left) and immediately (1 ps) after (right) relaxation of the crystal. For all of the monolayer compositions studied (acetate, oleate, and a 1:1 mixture of the two), the azimuthal distribution of the ligands is strongly peaked at 45° and -45° (Figure 2e), meaning that most of the carboxylate moieties are oriented with their O-O axis perpendicular or parallel to the [110] axis of the crystal (Figure 2d). The ligand tail length influences their polar orientation (Figure 2f), with acetate ligands having a peaked  $p(\theta)$  distribution. At the same time, monolayers that include oleic acid chains display a long tail distribution with a significant probability for their tail to be perpendicular to the surface. We found that acetate ligands bind to the Cd-rich (001) surfaces in two ways, shown in Figure 2c. In the bridging mode (i), the acetate molecule stands symmetrically on top of two Cd atoms. In contrast, in the tilting mode (ii), the acetate straddles a Cd atom asymmetrically, with one of the oxygens on top of the Cd atom and the other in the space between two Cd atoms. These two positions have preferred orientations: the first is observed along the dense Cd-Se-Cd rows (which are perpendicular to each other on the top and bottom facets, see Figure 2b). In contrast, the second position generally happens perpendicular to the dense rows. The dominant binding mode in our simulations is the tilting mode (ii), oriented perpendicular to the dense rows. This is also the preferred tilting mode predicted by DFT [19, 20], though Ref. [20] argues that a chelating mode is globally preferred. As discussed below, the direction in which the NPL bends appears to be inherent to the crystal structure, with the overall shape determined by the crystal orientation and dimensions and the ligand type.

## ELASTIC THEORY OF THIN SHEETS

When the ligands reach their equilibrium configuration, the NPL crystal is relaxed yielding insight into how it deforms under the effect of surface stresses induced by the ligands. We first consider square NPL with a 10 nm width and edges parallel to the [110] and  $[\bar{1}10]$  directions (Figure 3). The relaxed NPL displays a saddle shape, as can be seen in the MD snapshot (Figure 3a) and in the displacement field in Figure 3c. This characteristic shape has non-zero Gaussian curvature with a positive principal curvature direction along [110] and a negative principal curvature along  $[\bar{1}10]$ . Our simulations are thus consistent with the experimental observation of preferred bending along the [110] directions. To understand the origin of this deformation, we mapped the in-plane forces on the crystal atoms averaged over 100 fs to 300 fs after the beginning of the crystal deformation (Figure 3b). We track down the origin of the deformation to ligand-induced stresses on the top and bottom

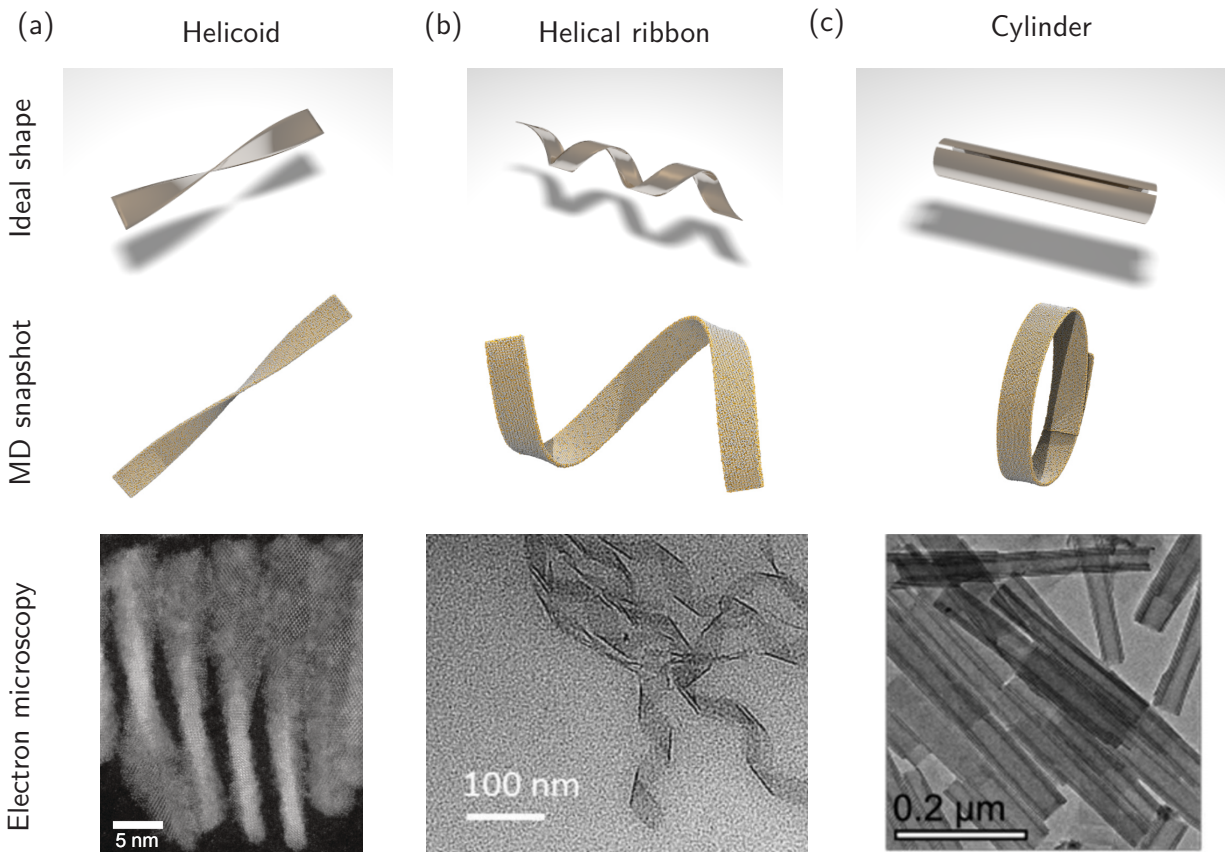


FIG. 1. CdSe colloidal nanoplatelet polymorphism. Three different shapes have been observed for CdSe NPL: (a) helicoids with a non-zero Gaussian curvature and a straight centerline, (b) helical ribbons with a helical centerline and a zero Gaussian curvature, and (c) tubes with a circular centerline and a zero Gaussian curvature. For each case, an idealized shape (top), a snapshot from an MD simulation (center) and an electron microscopy image (bottom) are shown. The MD simulation snapshots depict 3ML NPLs with a thickness of 1.1 nm and lateral dimensions of  $150 \text{ nm} \times 10 \text{ nm}$ . The TEM images are adapted from Refs. [4], [12], and [13].

surfaces, which are directionally anisotropic (Figure S1). The anisotropy in stress can also be seen in Figure S3, particularly in the case of the midplane. On the top surface, the anisotropic stress tends to bend the crystal in the  $[110]$  direction hence imposing a preferred positive curvature, while on the bottom surface, the stress direction is orthogonal and thus yields a preferred curvature along the  $[\bar{1}10]$  axis. Due to surface stress, a strain gradient appears along the  $[001]$  axis of the NPL, generating a spontaneous curvature.

The directional stress anisotropy between the top and bottom layers is due to the interplay between the crystalline structure of the NPL and the cutting planes at their top and bottom. The NPL synthesis involves carboxylates, X-type ligands that bind preferably to cations [21]. Hence, the top and bottom surfaces are cadmium-rich  $[001]$  surfaces. The improper rotation symmetry of the  $\bar{4}$  axis in the zinc blende ( $\bar{4}3m$ ) structure means that as we go from the top surface to the bottom, the Cd-Se bonds rotate by  $90^\circ$  for each monolayer added (Figure 2b). These bonds thus adopt a helical configuration

whose axis is oriented along the  $[001]$  direction. In the end, the Cd-Se bonds at the top and bottom of the NPL are always oriented orthogonal to each other. Chirality arises when the edges of the NPL are misaligned with the directions of preferred curvature, inducing twisting, and one edge is longer than the other, such that one handedness of twisting has lower energy than the other. This is further discussed in the next section. Note that the mid-plane of the NPL is not a mirror symmetry plane since the reflection of a Se atom in the bottom part corresponds to a vacant tetrahedral site in the top part. There are also no odd-even effects in the number of monolayers, with the preferred curvatures always orthogonal, whatever the number of monolayers, as shown in detail in Figure S4. This is consistent with twisted geometries observed for 3, 4 and 5 ML CdSe NPLs [3, 22].

Equilibrium configurations of NPL thus result from the minimization of elastic energy, with curvatures imposed at the top and bottom layers by the surfactant monolayer. This elasto-geometrical problem can be solved using the incompatible elasticity theory of thin sheets, in

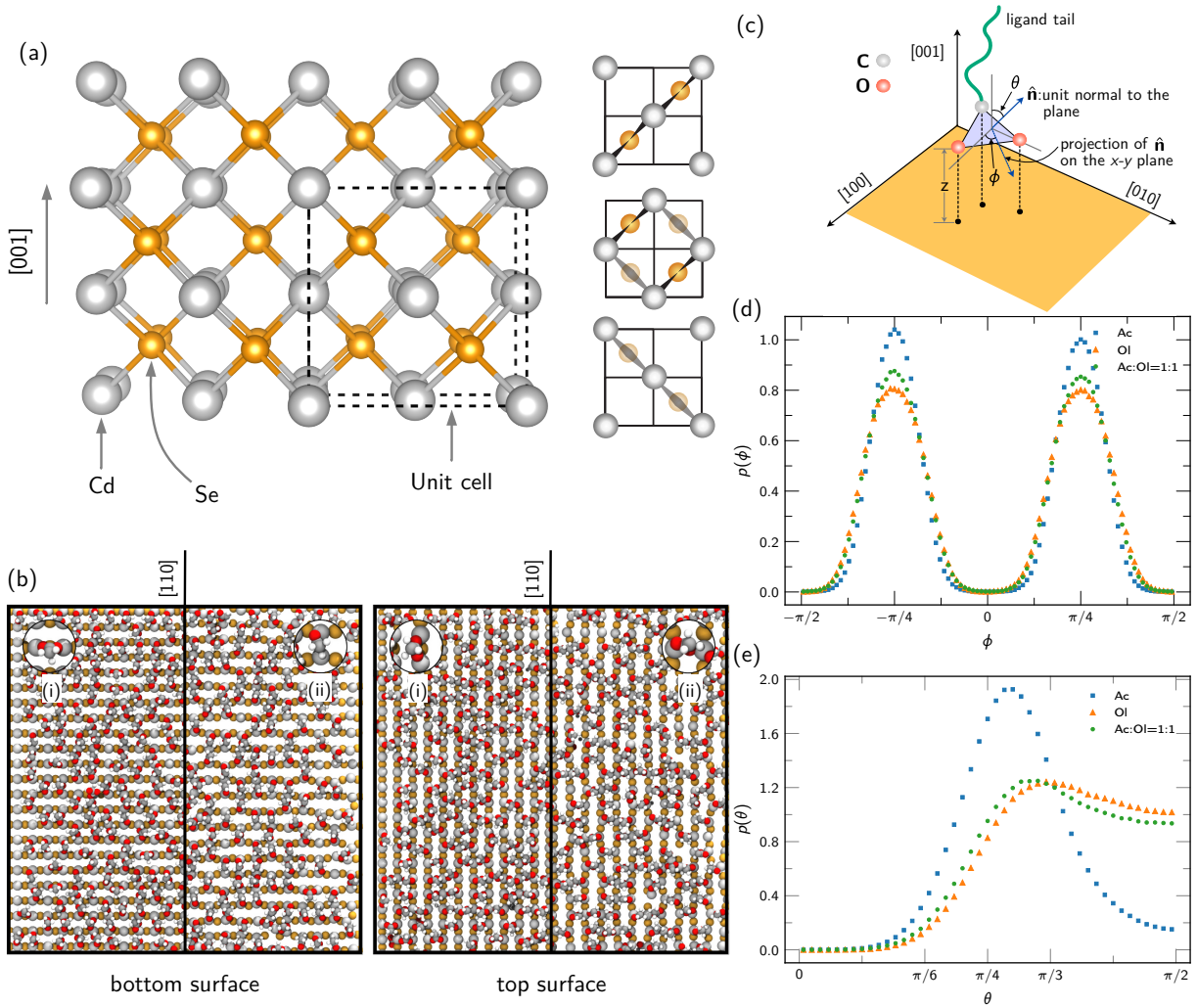


FIG. 2. Ligand interaction with the NPL surface. (a) Crystallographic structure of CdSe zinc-blende NPL. The top and bottom facets correspond to the (001) planes. (b) View along the [001] axis showing how Cd and Se atoms in adjacent layers are bonded. (c) Simulation snapshots of acetate ligands binding onto the top and bottom surfaces of a CdSe NPL (1.1 nm thick) along the [001] direction. (d) Schematic of the COO<sup>-</sup> binding moiety of acetate and oleate ligands on the surface of a CdSe NPL. The vector  $\hat{n}$  is the unit normal to the plane formed by the carbon and two oxygen atoms, which makes an angle  $\theta$  with the  $z$ -axis and whose projection on the  $xy$ -plane makes an angle  $\phi$  with the  $x$ -axis. The axes  $x$ ,  $y$ , and  $z$  represent the [100], [010], and [001] crystallographic directions.  $z$  is the perpendicular distance of an atom of the binding moiety from the  $xy$ -plane. Probability density functions of the angles  $\phi$  (e) and  $\theta$  (f) associated with the normal to the plane formed by the atoms of COO<sup>-</sup> for different ligands coating a CdSe NPL. The labels denote the following: Ac – acetate coated NPL; OI – oleate coated NPL; AcOI – 1:1 mixture of acetate and oleate.

which the total elastic energy is described as the sum of bending and stretching energies. The two terms can be expressed as a function of metric and curvature tensors and the material's mechanical properties. This framework has proven accurate in describing a wide variety of microscopic and macroscopic systems ranging from surfactant assemblies [23] to chiral seed pods [24]. In our case, the ligands dictate a curvature only at the top and bottom surfaces (Figure S1), while strains beyond the first atomic layers result from strain propagation along the NPL thickness towards the mid-plane. We developed a multi-layer model in the incompatible elasticity frame-

work, which features these boundary conditions (see theory section in the SI Appendix). The derived energy functional shows that NPL can be described as ribbons with a pure spontaneous twist, where the effective curvature is given by

$$\bar{\kappa} = \kappa_0 \Psi \frac{\Phi^3}{1 + \Phi^3}, \quad (1)$$

where  $\kappa_0$  is the curvature at the NPL/ligand interface,  $\Psi = Y_{\text{lig}}/Y_{\text{bulk}}$  is the ratio between the interfacial and bulk Young's moduli, and  $\Phi = e/t$  is the ratio between the effective thickness of the surfactant layer and the

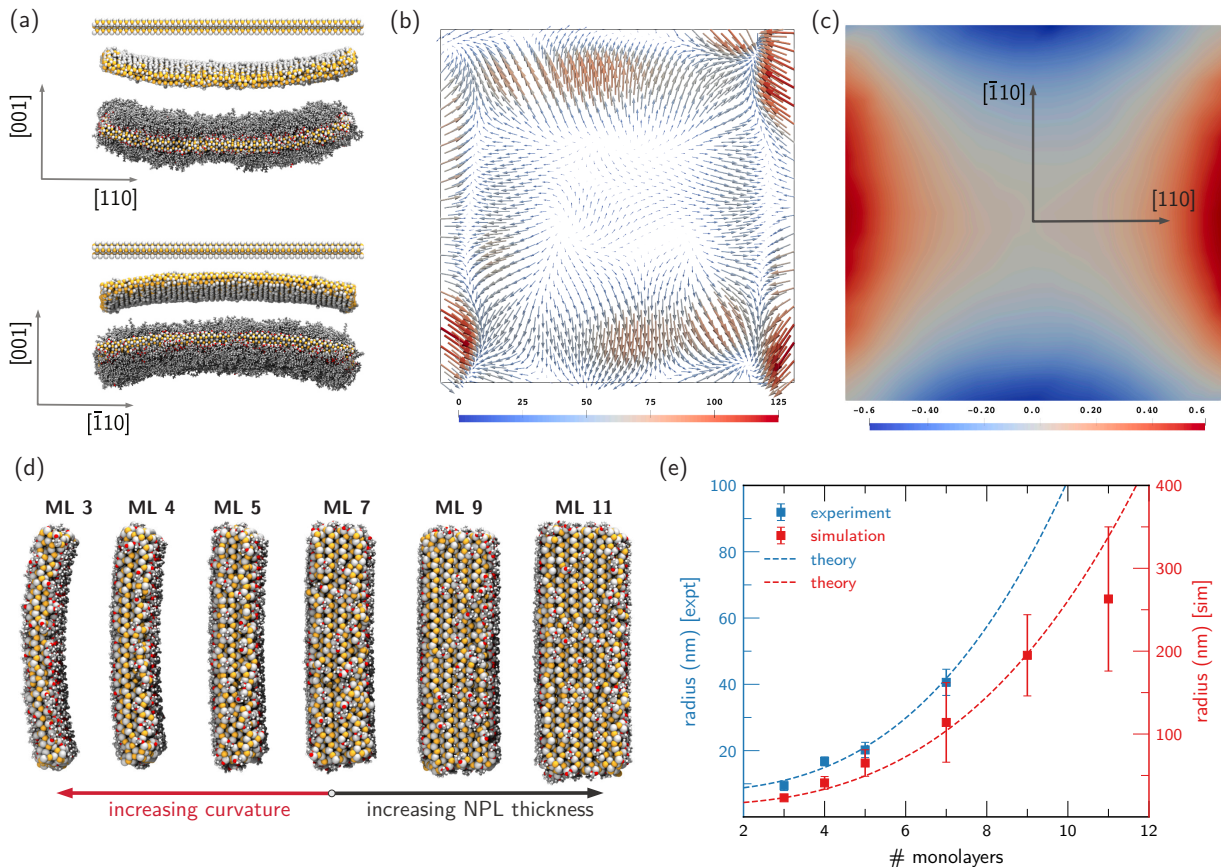


FIG. 3. (a) Simulation snapshots of a square 3 ML CdSe NPL with 10 nm edge length and thickness 1.1 nm. The two viewing directions illustrate the non-zero Gaussian curvature. (b) Spatial variation of in-plane forces (in pN) on the atoms of the midplane calculated by averaging over 100 fs to 300 fs after the commencement of deformation. The colors of the arrows indicate the magnitude of the forces. (c) Equilibrium displacement field of the NPL midplane (in nm) along the [001] direction. (d) Simulation snapshots for square NPL of increasing thickness (3 – 11 ML, i.e. 1.1 nm – 3.5 nm in thickness) from left to right. (e) The radius of curvature (nm) as a function of the number of monolayers in experiments and MD simulations. Experimental points come from Po *et al.* [5]. The dashed lines represent fits to Eq. 9 of the SI Appendix with fitted parameters  $\Psi\kappa_0 = 0.1328$  for experiments and 0.0712 for simulations and  $e = 2.752$  nm for experiments and 2.456 nm for simulations.

NPL thickness.

## COMPARISON WITH SIMULATION RESULTS

To test the scaling between the effective curvature and the thickness, we simulated 10 nm by 10 nm square NPL and calculated their radii of curvature along the  $[110]$  and  $[\bar{1}10]$  directions as a function of NPL thickness (for acetate ligands). Results from these simulations, as well as similar experiments [5], are shown in Figure 3e. While there are numerical differences between the two, this is not surprising given the experiments were done on much larger NPL that lie in the stretching-dominated regime and form tubes with cylindrical curvature rather than saddle shapes. Fitting the variation of curvature with thickness to Equation 1 with two unknown parameters yields an excellent fit with very similar values for the effective thickness of the surfactant layer  $e$ , which is, as

expected, of the same order of magnitude as the thickness of the NPL. The larger deviation observed for the  $\kappa_0\Psi$  prefactor between experiments and simulations can be explained by the difference in experimental and simulation size regimes, as noted above. Other possible contributions could be the accuracy of the force field used to describe the ligand-surface interactions or uneven ligand coverage between the NPL surfaces in experiments [25]. Still, the overall agreement between theory, experiment and MD simulations proves the relevance of our model in grasping the key physical ingredients at play.

An important parameter for shape selection in incompatible elastic ribbons is the angle between the principal direction of curvature and the ribbon’s longitudinal axis. Since we previously showed that ligands induce principal curvatures in the  $[110]$  and  $[\bar{1}10]$  directions, we define  $\alpha$  as the angle between the long edge of the NPL and the  $[110]$  axis. Figure 4a shows simulation snapshots for  $\alpha$  varying from 0 to  $\pi/2$  for NPL with a ribbon geometry ( $L_x = 10$

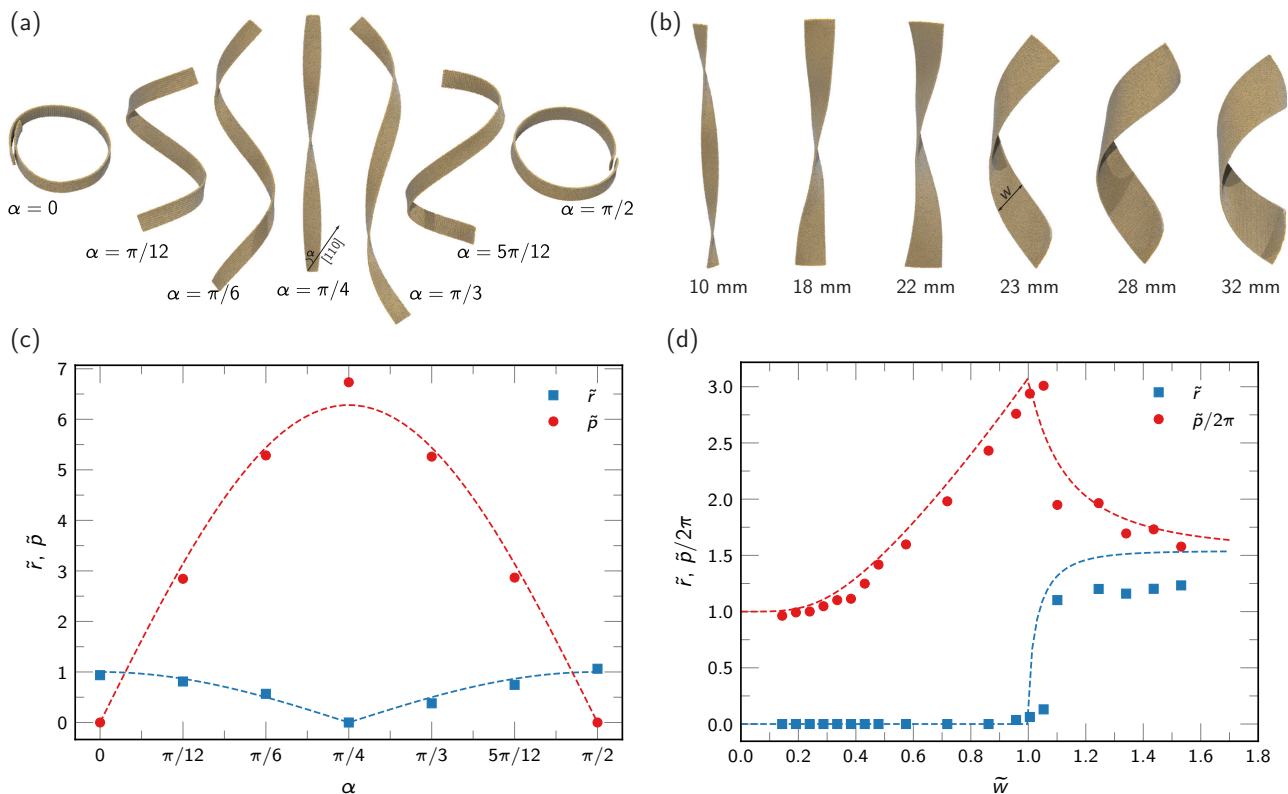


FIG. 4. (a) Snapshots of 3ML CdSe NPL conformations from MD simulations as a function of the angle  $\alpha$  between the [110] crystallographic direction and the long edge of the NPL. The NPL are 200 nm long (except for  $\alpha = \pi/4$ , which is 150 nm) and 10 nm wide with a thickness of 1.1 nm, coated with a 1:1 mixture of acetate and oleate ligands (not shown for clarity). (b) Radius and pitch of the NPLs in (a) as a function of the angle  $\alpha$ , along with theoretical predictions (dashed lines) from Armon *et al.* [26] (c) Snapshots of CdSe NPL conformations from MD simulations for different widths at a fixed angle  $\alpha = 45^\circ$  between the [110] crystallographic direction and the long edge of the NPL. The NPLs are 150 nm long with a thickness of 1.1 nm and coated with acetate ligands (not shown for clarity). (d) Radius and pitch for NPL similar to those in (c) as a function of width at  $\alpha = \pi/4$ , along with theoretical predictions (dashed lines) from Grossman *et al.* [27] (see Sec. 1.4 for details).

nm and  $L_y = 100$  nm) covered in a 1:1 mixture of oleate and acetate ligands. The helicoid is the favoured geometry for  $\alpha = \pi/4$ . As the angle increases towards  $\pi/2$  (or decreases towards 0), the shape unwinds to finally reach a circular tube-like shape for  $\alpha = \pi/2$  (or 0). For chiral shapes, corresponding to  $\alpha \neq \pi/2$  or 0, the two enantiomers are obtained for  $\pi/2 - \alpha$  and  $\pi/2 + \alpha$ . We stress that shapes corresponding to  $\pi/4 - \alpha$  and  $\pi/4 + \alpha$  are not enantiomorphs since one can be obtained from the other by a simple rotation. From the equilibrated shapes, we extract the pitch  $p$  and radius  $r$  (see Methods) and report them as a function of  $\alpha$  in Figure 4c. For narrow strips, i.e., in the limit where the width  $w \rightarrow 0$ , Armon *et al.* [26] derived the relations  $\tilde{r} = \cos 2\alpha$  and  $\tilde{p} = 2\pi \sin 2\alpha$ , where  $\tilde{r} = \bar{\kappa}r$  and  $\tilde{p} = \bar{\kappa}p$  are the reduced radius and pitch, respectively. Fitting the extracted values from the simulation to these relations yields an excellent fit with the only free parameter  $\bar{\kappa} = 3.35 \times 10^{-2} \text{ nm}^{-1}$ .

The hallmark feature of ribbons bearing incompatible curvatures is a second-order phase transition between a helicoidal shape for small widths into a helical shape as

the width increases. The stretching energy scales as  $w^5$  whereas the bending energy scales like  $w$ . Hence, when the width reaches a critical value, it becomes energetically favorable to unwind the helicoid and transition to a helical shape (or spiral) where the Gaussian curvature is expelled. In this geometry, the stretching energy term dominates and NPL behave as ribbons with a single intrinsic curvature that would be obtained by stretching only one side (top or bottom). Figure 4b shows the shape evolution with increasing width  $w$  at  $\alpha = \pi/4$  for NPL with a ribbon geometry ( $L_y = 150$  nm) covered with acetate ligands. We observe a clear transition between helicoidal ribbons at low  $w$  and helical ribbons as the width increases. From the simulated shapes, we extract the pitch  $p$  and radius  $r$  (see Methods) and report them as a function of the reduced width  $\tilde{w} = w/w_c$  in Figure 4d. The unwinding transition occurs for a critical width  $w_c \approx 23$  nm for  $\nu = 0.35$ ,  $t = 1.1$  nm with  $\bar{\kappa} = 4.65 \times 10^{-2} \text{ nm}^{-1}$  as the only fitting parameter for  $\tilde{r}$  and  $\tilde{p}$  as a function of  $\tilde{w}$  to equations in [27]. The small difference in  $\bar{\kappa}$  between the two figures points towards

the role of the ligand tails on the reference curvature with pure acetate ligands allowing a larger  $\bar{\kappa}$  than mixed oleate/acetate. Furthermore, we retrieve in simulations the asymptotic behaviours predicted by theory: in the narrow limit the pitch  $\tilde{p}^\dagger = 2\pi$ , and in the wide limit the pitch  $\tilde{p}^\dagger = 2\pi/(1-\nu)$  and the radius  $\tilde{r}^\dagger = 1/(1-\nu)$ .

## EFFECTIVE CURVATURE

The fact that all the simulated data can be fitted with only one free parameter  $\bar{\kappa}$ , both for variations in  $\alpha$  and  $w$ , is remarkable. This unique parameter encodes the interaction between the ligands and the crystal surface. Different ligand head-groups and binding motifs affect the imposed curvature at the interface as shown experimentally for CdSe [6] and CdTe [7]. This effect is also observed in our MD simulations, where 5ML NPL coated with butanethiol (see Figure S2) displays a much smaller radius of curvature (28 nm) than the same NPL coated with acetate (77 nm, see Figure 3e). The greater curvature induced by the thiol ligands in our simulations is consistent with the experimental observation that flat 5-6 ML CdTe NPL roll up when their oleic acid ligands are replaced with hexadecanethiol [7].

More surprisingly,  $\bar{\kappa}$  also depends on the interactions between the ligand tails, which includes enthalpic contributions due to van der Waals interactions and entropic effects related to the free volume available for the ligand chains in the monolayer to undergo conformational changes. In simulations, the critical role of repulsive entropic interactions between ligands is evidenced by curvature variations observed when the  $\epsilon$  parameter (which tunes the strength of vdW attraction between the tails) is changed. For example, for 3 ML 20 nm  $\times$  10 nm CdSe NPLs at 100 K, on reducing  $\epsilon$  from 100% to 50%, the radius of curvature of the NPL midline changes from 43.5 nm to 36.9 nm for octanoate ligands. In addition, when the chain length of linear thiolate ligands increases from 4 to 18 carbons, we observe a significant decrease in curvature in MD simulations, in semi-quantitative agreement with experiments (see Figure S2). Shapeshifting is even more dramatic when a branched ligand is used. Helical NPL initially coated with carboxylates undergo complete unfolding when functionalized with 2-ethyl-1-hexane thiol (see Figure S5), showing that entropic interactions between ligand tails play a key role in determining NPL shape.

## CONCLUSION AND PERSPECTIVES

In this study, we demonstrated that the natural curvature of CdSe NPL is due to interaction between ligands and the NPL crystal. This interaction induces directionally anisotropic surface stresses, leading to preferred curvature along different crystallographic axes on the top and bottom surfaces. The angle between the

NPL edge and these axes defines its chirality, while the balance of bending and stretching energies relative to the NPL's width and thickness determines its shape.

We traced back this effect's origin to the NPL's crystallographic structure. Both top and bottom surfaces of the NPL are cadmium rich (001) planes and the symmetry elements of the zinc-blende structure lead to orthogonally oriented Cd-Se bonds on these surfaces. The shape of NPLs composed of other materials could be explained by this theoretical framework if they exhibit similar structural features. For example, other zinc-blende NPLs may exhibit frustrated curvature effects [7]. More generally, we predict that NPLs that have a crystal structure with a  $\bar{6}$ ,  $\bar{4}$  or  $\bar{3}$  symmetry axis suitable oriented to their cutting planes have the potential to exhibit such behavior. This prediction is consistent with a recent report of chiral Gd<sub>2</sub>O<sub>3</sub> NPLs [28]. Cubic Gd<sub>2</sub>O<sub>3</sub> belongs to the Ia $\bar{3}$  space-group which has a  $\bar{3}$  symmetry axis and, interestingly, these NPL exhibit helical geometry in some instances. Chirality can also be achieved for more symmetric crystal structures via the use of chiral ligands. For example, gold has been shown to display twisted ribbon geometries when functionalized with chiral thiols [1].

Another intriguing possibility is to use this new insight to design NPL that can undergo large shape changes in solution with marginal changes in the structure of the NPL/monolayer interface. Close to the unwinding transition ( $w \simeq w_c$ ), dramatic shape changes are expected to occur upon small  $\bar{\kappa}$  changes. Since this parameter depends on the molecular details of the self-assembled monolayer, we expect that changing the chemical identity of the surfactants, e.g. via ligand exchange, could drive such a shape change. Another feature of this class of systems is bistability [29], meaning that two geometrically different conformations can have the same energy. It should thus be possible to go from one configuration to the other with minimal energy input to the system. This feature could be exploited in stimuli-responsive nanomaterials by applying the theory and physical insights described in this paper, linking the molecular structure of ligands with the morphology of inorganic NPL.

## ACKNOWLEDGMENTS

This article is part of a project that has received funding from the European Research Council (ERC) under the European Union's Horizon 2020 research and innovation program (Grant agreement No. 865995). Part of this work was supported by the Australian Research Council through the Centre of Excellence in Exciton Science (CE170100026). Computational resources were provided by the University of Sydney HPC service and the Pawsey Supercomputing Centre with funding from the Australian Government and the Government of Western Australia. We thank Efi Efrati, Arezki Boudaoud, Yoël Forterre and Lydéric Bocquet for stimulating discussions. We thank Sandrine Ithurria for providing some data of

Ref. 5 before publication. This work was granted access to the HPC resources of IDRIS under the allocation 2022-AD010913529 made by GENCI. We also gratefully acknowledge support from the PSMN (Pôle Scientifique de Modélisation Numérique) computing centre of ENS de Lyon.

## MATERIALS AND METHODS

### A. Synthesis and functionalisation of CdSe Nanoplatelets

#### 1. Synthesis of 3ML CdSe NPLs

In a typical synthesis, 140 mL ODE, 2.22 g Cd(Acetate) $\cdot$ 2 $\cdot$ 2H $_2$ O and 2.23 mL oleic acid are introduced in a 250 mL three-neck flask. The temperature of the solution is raised to 200°C under Argon flux. After injection of 3.6 mL of TOPSe 1M, the reaction mixture is annealed at the same temperature for 10 minutes, forming 3 MLs CdSe NPLs. At the end of the reaction, 10 mL of oleic acid is added before the solution cools down to room temperature. NPLs are isolated from the reaction mixture by centrifugation; they are then dispersed in hexane and precipitated one more time by adding ethanol. The final product is dispersed in hexane.

#### 2. Functionalisation by thiols

200  $\mu$ L of the previous 3ML CdSe NPL dispersion are added to 1mL of toluene. 1 mmol (large excess amount) of the appropriate thiol is added, and the solution is heated for three days at 65°C. The NPLs are precipitated by adding ethanol, the dispersion is centrifuged at 9000 rpm for 3 minutes and the precipitate is redispersed in toluene. The purification step is repeated once.

### B. Molecular dynamics simulations

Molecular dynamics (MD) simulations of isolated ligand-coated CdSe NPL were performed at constant volume and temperature (100 K for thiol-coated NPL and 300 K for the remaining systems), maintained via a Nosé-Hoover thermostat, using the LAMMPS software package [30]. The NPL and ligands were modeled with explicit atoms, while the solvent was treated implicitly, in order to limit computational costs, by reducing the interaction strength between ligand chains to 85% (3ML oleate-coated NPL) and 50% (5ML thiol-coated NPL) of their original value. These values were chosen based on results from previous work with alkanethiols coating spherical nanoparticles [31] and on the fact that ligand chains remained disordered and mobile at the chosen temperature. Following Rabani [32], the interaction potential for CdSe consists of a short-ranged 12-6 Lennard-

Jones potential combined with a long-range Coulombic contribution, with parameters given in Ref. 32. Ligand interactions were modeled using the OPLS-AA force field [33]. The set of parameters for each type of ligand were obtained from the LigParGen web server [34–36]. The MD equations of motion were integrated using the velocity-Verlet algorithm with a time step of 1 fs.

CdSe NPL with Cd-terminated [001] polar surfaces (see Fig. 2a) were constructed by first placing the Cd and Se atoms on a zinc blende lattice (see SI Appendix for calculation of the lattice parameter). The structures thus obtained were cut by a set of parallel planes along the crystallographic axes to obtain the desired sizes and the number of monolayers. For NPL with different orientations of the [110] axis, the lattice was rotated by appropriate angles prior to cutting. Next, the crystalline core was coated with either acetate, oleate, or thiolate ligands at a density of 3.27 ligands nm $^2$ , which ensured charge neutrality of the NPL. The coating was performed by randomly placing the ligands within a thin shell encompassing the core and then optimizing their positions using the software package PACKMOL [37].

The resulting ligand-coated core was placed at the center of a simulation box, with at least 50 Å of vacuum added on all sides. In almost all cases, the simulation box was a rectangular parallelepiped, where the longest and shortest dimensions were of the order of the associated NPL dimensions in their undeformed state. This ensured that in practice, after equilibration, the box dimensions remained significantly larger than the NPL size. Periodic boundary conditions were applied along all three dimensions.

Equilibration was performed *via* a sequence of stages. First, an energy minimization run was carried out to remove any significant overlap of the atoms. Second, the ligands were relaxed at constant energy with a maximum atomic displacement of 0.1 Å per time step for a duration of 50 ps. Third, the ligands were relaxed at the desired temperature for another 100 ps. Note that during the above three stages, only the atoms belonging to the ligands were displaced and the CdSe core was held static. Finally, both the ligands and the crystalline core were allowed to equilibrate together at the chosen temperature for 6 ns. Equilibration was followed by a production run of 3-25 ns, depending on the NPL size and whether significant fluctuations persisted in the resulting configurations. The configurations were sampled every 10 ps. All results presented here have been averaged over all the sampled configurations.

### C. Characterisation of bulk elastic constants

The deformation of CdSe NPL depends in part on the elastic properties of the underlying zincblende CdSe lattice, which has not been determined experimentally. For reference, we therefore report the bulk elastic constants for this lattice under several thermodynamic conditions

TABLE I. Calculated lattice constants  $a$  (in Å), elastic constants  $C_{ij}$  (in GPa), and bulk moduli  $B$  (in GPa) of zincblende CdSe. Results obtained from Eran Rabani at 0 K are compared with our results at the same volume and temperature (NVT) and at 1 atm pressure (NPT). The experimental lattice constant is 6.08 Å [38].

Property	Rabani (0 K)	NVT (0 K)	NPT (0 K, 1 atm)	NPT (300 K, 1 atm)
$a$	6.13	6.13	6.17	6.20
$C_{11}$	53.8	53.6	53.3	53.2
$C_{12}$	40.2	39.0	38.5	40.4
$C_{44}$	24.1	24.0	23.1	38.1
$B$	44.7	44.0	43.5	44.6

using the same potential used to simulate the NPL (see Table I). These values were reported incorrectly in prior work, [32, 39] so for comparison we list values provided directly to us by Eran Rabani.

The bulk elastic constants were determined by placing a cubic 3D crystal inside a periodic simulation box, letting it equilibrate, and then measuring changes in the stress tensor as the box was deformed. Three different cases were considered: a temperature of 0 K and constant volume (to match the lattice constant reported previously) [39]; a temperature of 0 K and a pressure of 1 atm; and at a temperature of 300 K and a pressure of 1 atm. The temperature and pressure were maintained using a Nosé-Hoover thermostat and barostat, respectively.

#### D. Characterization of NPL shape

At equilibrium, ligand-coated CdSe NPL adopt deformed conformations that possess either a helicoidal midplane or a helical midline. Such shapes can be characterized by their radius and pitch. However, the calculation of these quantities directly from atomic positions is cumbersome and prone to excessive noise in the data. To alleviate these issues, we employed an approach based on an atom-to-continuum mapping to extract the midplane and the midline in the form of a surface mesh and line mesh, respectively. Our approach has been informed and influenced by several works in the solid mechanics community [40–46], where the primary emphasis was on calculating inhomogeneous continuum fields, e.g., strain and stress, from molecular dynamics simulations.

We considered the undeformed state of an NPL as a reference configuration with respect to which any deformation will be calculated. Since we are interested in only the midplane and the midline, it was sufficient to consider only the crystalline CdSe core. We constructed a three dimensional grid spanning the region in space occupied by the Cd and Se atoms. To reduce the number of grid points as well as to improve the accuracy of the subsequent interpolations, the grid points were chosen to be Chebyshev-Gauss-Lobatto nodes, appropriately mapped from the unit domain  $[-1, 1] \times [-1, 1] \times [-1, 1]$ . Atomic displacements were calculated, for each Cd and Se atom, from their positions in the reference and the deformed

states. Next, the atomic displacements were projected onto the grid points via a localization function. The localization function  $\psi$  is a regularized approximation with compact support to a  $\delta$ -function that averages any atomic property over the neighboring atoms of a grid point. Its functional form is that of a quartic spline (see Eq (4.5) in Ref. 43):

$$\psi = \begin{cases} \frac{105}{16\pi r_w^3} \left(1 + \frac{3r}{r_w}\right) \left(1 - \frac{r}{r_w}\right)^3 & \text{if } r \leq r_w, \\ 0 & \text{otherwise,} \end{cases} \quad (2)$$

where the support radius  $r_w$  was taken equal to 8 Å for calculating the displacement field and 20 Å for the force and stress fields. While the exact value of  $r_w$  is subject to choice, a higher value will increase computational cost, and too low a value will result in poor spatial averaging. The chosen value of 8 Å is greater than the size of the CdSe unit cell, and varying it generated only minor changes in any subsequent calculations. However, atomic forces and stresses being highly fluctuating quantities both spatially and temporally, we had to increase  $r_w$  to approximately three unit cells in order to obtain a smoother field. Note that  $\psi$  is defined in terms of the coordinates of the reference configuration, hence after projecting the atomic displacements onto the reference grid the resulting continuum displacement field is a material field [41]. Furthermore, following Zimmerman et al [41], we used a mass-weighted average when calculating all field quantities from the respective atomic quantities.

The displacement field was averaged over all NPL configurations sampled over a simulation run, and then interpolated to the midplane and the midline. These interpolations were performed onto a uniform grid in two and one dimensions, respectively. The nodal coordinates of deformed state of the midplane and midline were directly obtained by adding the nodal displacements to the nodal positions in the reference state. From the nodal coordinates of the deformed midplane, the nodal surface normals were calculated by averaging the normals to all quadrilaterals incident onto a node.

The pitch of helicoidal midplanes was obtained by the kinematic surface fitting method presented in Refs. 47 and 48. In this case, an NPL undergoes pure twisting, hence the radius is zero. In addition to the

nodal positions, the fitting algorithm also requires the nodal surface normals. For NPL with a helical midline, their radii were determined by fitting a cylinder to the coordinates of the midline using the orthogonal distance regression method discussed in Ref. 49. The fitting algorithm requires an initial estimate for the axial direction of the helix and the radius. The former was determined from a combination of singular value decomposition of the midline coordinates and visual inspection. Next, to obtain an estimate of the radius, the coordinates were projected onto a plane perpendicular to the axis and fit to a circle using Taubin's method [50, 51]. The fit to a cylinder yields the final values of the radius and the helix axis. Finally, the pitch was obtained from the linear relation between the axial and the angular displacements on traversal along the midline.

For square ligand-coated CdSe NPL that bent along the [110] and  $\bar{1}\bar{1}0$  directions adopting a saddle shape geometry, we calculated surface curvatures by fitting a circular arc to the inner layers of atoms of the crystals. We fitted a circle to the line of atoms of interest by employing an orthogonal least squares algorithm in which the sum of squares  $f = \sum_{i=1}^n d_i^2$  is minimized. In this equation,  $d_i$  is the geometric distance between the data point of choice  $(x_i, y_i)$  and the hypothetical circle, and is given by  $d_i = x_i - a_2 + y_i - b_2 - R$ , where  $(a, b)$  is the center of the circle, and  $R$  is its radius. We used Taubin's method to minimize  $f$  algebraically [50], taking only the inner layers of atoms in a NPL into account to reduce error, as atoms directly in the surface of the crystal tend to be more disordered due to their strong interaction with ligands making quantification of the curvature more difficult. Additionally, we removed gross outliers if those were still present [52].

### E. In-plane forces calculation

The in-plane forces for Cd layers were averaged within each quadrant of the acetate-coated NPL (Figure S1) over the interval between 100 fs to 300 fs following crystal relaxation in the NVT ensemble at 100 K. This step was preceded by a 1 ps-long ligand relaxation stage, where ligands were allowed to find their preferred position on the surface of the fixed crystal in the absence of solvent.

### F. Theory

We consider a ligand-coated NPL as a multilayered ribbon of length  $L$  and width  $w$ . The ribbon consists of a crystalline core of thickness  $t$ , bounded by two layers of ligands at the top and the bottom, each of effective thickness  $e$ . The crystalline core is in turn composed of  $N$  layers, each of uniform thickness  $t_{\text{single}}$ , and thus  $t = Nt_{\text{single}}$ . We further assume that  $L \gg w \gg (t + 2e)$ . In a typical experiment,  $e$  exceeds  $t_{\text{single}}$  by a factor of at

least five. At the top and the bottom, a unidirectional curvature of magnitude  $\kappa_0$  is induced by the interactions the ligands. The reference curvature  $\bar{\mathbf{b}}_{\pm}$  at the edges is given by

$$\bar{\mathbf{b}}_{\pm} = \pm \kappa_0 \begin{pmatrix} \cos^2 \alpha_{\pm} & \cos \alpha_{\pm} \sin \alpha_{\pm} \\ \cos \alpha_{\pm} \sin \alpha_{\pm} & \sin^2 \alpha_{\pm} \end{pmatrix}, \quad (3)$$

where  $\pm$  indicates the top (+) or bottom (-) layers and  $\alpha_{\pm}$  are the directions of the curvature relative to the ribbon midline. Since the top and the bottom are the same up to an orientation,  $\alpha_- = -\alpha_+$ . Henceforth we will assume  $\alpha_+ = \pi/4$ . Thus

$$\bar{\mathbf{b}}_{\pm} = \frac{\kappa_0}{2} \begin{pmatrix} \pm 1 & 1 \\ 1 & \pm 1 \end{pmatrix}.$$

Without the edges, the ribbon's bulk energy density is given by [27]

$$\begin{aligned} E_{\text{bulk}} &= Y_{\text{bulk}} \left[ \frac{tw^5}{80} (ln - m^2)^2 + \frac{t^3w}{3} \left\{ (l+n)^2 \right. \right. \\ &\quad \left. \left. - 2(1-\nu)(ln - m^2) \right\} \right] \\ &= Y_{\text{bulk}} \left[ \frac{tw^5}{80} \det \mathbf{b}^2 + \frac{t^3w}{3} \left\{ \text{Tr}^2 \mathbf{b} \right. \right. \\ &\quad \left. \left. - 2(1-\nu) \det \mathbf{b} \right\} \right], \end{aligned} \quad (4)$$

where  $Y_{\text{bulk}}$  is the Young's modulus of the bulk crystal,  $\nu$  is the Poisson's ratio, and  $l, m, n$  are the normal curvature, twist, and binormal curvature, at the midsurface, i.e.  $\mathbf{b} = \begin{pmatrix} l & m \\ m & n \end{pmatrix}$ .

Assuming the length scale of curvature to be much greater than that of the thickness, the curvatures at the top and bottom surfaces can be obtained from the curvature at the mid-surface as

$$\begin{aligned} \mathbf{b}_{\pm} &= \mathbf{b} \mp \frac{t}{2} \mathbf{b}^2 \\ &= \begin{pmatrix} l & m \\ m & n \end{pmatrix} \mp \frac{t}{2} \begin{pmatrix} l^2 + m^2 & m(l+n) \\ m(l+n) & m^2 + n^2 \end{pmatrix}. \end{aligned} \quad (5)$$

Thus the top and bottom surfaces of the ribbon contribute additional energy stemming from the difference between the curvature and the reference curvatures  $\bar{\mathbf{b}}_{\pm}$ . As the thickness of the ligands is larger than that of a single layer the top and bottoms ribbons additional contribution to the energy density is given, to leading order by

$$\begin{aligned} \Delta E &= Y_{\text{lig}} \left[ \frac{ew^5}{40} (ln - m^2)^2 + \frac{e^3w}{3} \left\{ \text{Tr}^2 (\mathbf{b}_+ - \bar{\mathbf{b}}_+) \right. \right. \\ &\quad \left. \left. - 2(1-\nu) \det (\mathbf{b}_+ - \bar{\mathbf{b}}_+) + \text{Tr}^2 (\mathbf{b}_- - \bar{\mathbf{b}}_-) \right. \right. \\ &\quad \left. \left. - 2(1-\nu) \det (\mathbf{b}_- - \bar{\mathbf{b}}_-) \right\} \right] \end{aligned} \quad (6)$$

where  $Y_{\text{lig}}$  is the Young's modulus of the outer ribbons. Using a little algebra, the additional term can be written, to leading order (assuming the curvature is much greater compared to the thickness)

$$\Delta E = 2Y_{\text{lig}} \left[ \frac{ew^5}{80} (\det \mathbf{b})^2 + \frac{e^3 w}{3} \left\{ \text{Tr}^2 (\mathbf{b} - \mathbf{B}) - 2(1 - \nu) \det (\mathbf{b} - \mathbf{B}) + (1 + \nu) \kappa_0^2 \right\} \right] \quad (7)$$

where  $\mathbf{B} = \begin{pmatrix} 0 & \kappa_0 \\ \kappa_0 & 0 \end{pmatrix}$ . Note that the last term is a constant that may be discarded from the energy as it does not contribute to the mechanics. Finally, introducing the thickness ratio  $\phi = e/t$  and the energy ratio  $\psi = Y_{\text{lig}}/Y_{\text{bulk}}$  we may write the total effective energy density as

$$\begin{aligned} E &= E_{\text{bulk}} + \Delta E \\ &= Y_{\text{bulk}} \left[ \frac{(1 + \psi\phi) tw^5}{80} (\det \mathbf{b})^2 + \frac{t^3 w}{3} \left\{ \text{Tr}^2 (\mathbf{b} - \bar{\mathbf{b}}) - 2(1 - \nu) \det (\mathbf{b} - \bar{\mathbf{b}}) \right\} \right] + E_0 \end{aligned} \quad (8)$$

where  $\bar{\mathbf{b}} = \frac{\psi\phi^3}{1+\phi^3} \mathbf{B}$  is the effective reference curvature, and

$$E_0 = 2Y_{\text{lig}} \frac{e^3}{3} w \left[ (1 + \nu) \kappa_0^2 + \frac{\phi^2}{1 + \phi^3} \left\{ \text{Tr}^2 \mathbf{B} - 2(1 - \nu) \det \mathbf{B} \right\} \right] \quad (9)$$

is the residual energy that does not affect the mechanics. The energy in (8) has the same form as that of a general ribbon with residual stress [27], which indicates that the system behaves as a ribbon with a spontaneous twist with an effective curvature  $\bar{\kappa} = \psi\kappa_0\phi^3/(1 + \phi^3)$ . The radius of curvature can then be rewritten as:

$$r_c = \frac{1}{\psi\kappa_0} \left( 1 + \left( \frac{t}{e} \right)^3 \right). \quad (10)$$

The critical width  $w_c$  of a ribbon for helicoid-helix transition is [23, 27]

$$w_c = \left[ \frac{320}{3} \frac{1 + \nu}{(1 - \nu)^2} \right]^{1/4} \sqrt{\frac{t}{\bar{\kappa}}}, \quad (11)$$

Note that a similar formula given in Ref. 53 (Eq. 6a) has the signs flipped in the numerator and denominator due to a difference in geometry. Following earlier works [23, 26, 27, 29, 53] we express the NPL width  $w$ , pitch  $p$ , and radius  $r$  in their nondimensionalized form  $\tilde{p} = p\bar{\kappa}$ ,  $\tilde{r} = r\bar{\kappa}$ , and  $\tilde{w} = w/w_c$ . For narrow strips, i.e., in the limit  $\tilde{w} \rightarrow 0$ , the radius and pitch are given by [26]

$$\begin{aligned} \tilde{r} &= \cos 2\alpha \\ \tilde{p} &= 2\pi \sin 2\alpha. \end{aligned} \quad (12)$$

For wide strips with  $\alpha = \pi/4$  the asymptotic values of the radius and pitch are [26]

$$\tilde{r} = \frac{\tilde{p}}{2\pi} = \frac{1}{1 - \nu}. \quad (13)$$

- [1] W. Jiang, Z.-b. Qu, P. Kumar, D. Vecchio, Y. Wang, Y. Ma, J. H. Bahng, K. Bernardino, W. R. Gomes, F. M. Colombari, A. Lozada-Blanco, M. Veksler, E. Marino, A. Simon, C. Murray, S. R. Muniz, A. F. de Moura, and N. A. Kotov, Emergence of complexity in hierarchically organized chiral particles, *Science* **368**, 642 (2020).
- [2] B. T. Diroll, B. Guzelturk, H. Po, C. Dabard, N. Fu, L. Makke, E. Lhuillier, and S. Ithurria, 2D II–VI Semiconductor nanoplatelets: From material synthesis to optoelectronic integration, *Chem. Rev.* **123**, 3543 (2023).
- [3] L. Guillemeney, L. Lermusiaux, G. Landaburu, B. Wagnon, and B. Abécassis, Curvature and self-assembly of semi-conducting nanoplatelets, *Commun. Chem.* **5**, 1 (2022).
- [4] S. Jana, M. d. Frutos, P. Davidson, and B. Abécassis, Ligand-induced twisting of nanoplatelets and their self-assembly into chiral ribbons, *Sci. Adv.* **3**, e1701483 (2017).
- [5] H. Po, C. Dabard, B. Roman, E. Reyssat, J. Bico, B. Baptiste, E. Lhuillier, and S. Ithurria, Chiral helices formation by self-assembled molecules on semiconductor flexible substrates, *ACS Nano* **16**, 2901 (2022).
- [6] M. Dufour, J. Qu, C. Greboval, C. Méthivier, E. Lhuillier, and S. Ithurria, Halide ligands to release strain in cadmium chalcogenide nanoplatelets and achieve high brightness, *ACS Nano* **13**, 5326 (2019).
- [7] R. B. Vasiliev, E. P. Lazareva, D. A. Karlova, A. V. Garshev, Y. Yao, T. Kuroda, A. M. Gaskov, and K. Sakoda, Spontaneous folding of CdTe nanosheets induced by ligand exchange, *Chem. Mater.* **30**, 1710 (2018).
- [8] R. Ghafouri and R. Bruinsma, Helicoid to spiral ribbon transition, *Phys. Rev. Lett.* **94**, 138101 (2005).
- [9] R. L. B. Selinger, J. V. Selinger, A. P. Malanoski, and J. M. Schnur, Shape selection in chiral self-assembly, *Phys. Rev. Lett.* **93**, 158103 (2004).
- [10] G. M. Grason, Perspective: Geometrically frustrated assemblies, *J. Chem. Phys.* **145**, 110901 (2016).
- [11] D. M. Hall, M. J. Stevens, and G. M. Grason, Building blocks of non-euclidean ribbons: Size-controlled self-assembly via discrete frustrated particles, *Soft Matter* **19**, 858 (2023).
- [12] Y. Liu, N. Rowell, M. Willis, M. Zhang, S. Wang, H. Fan, W. Huang, X. Chen, and K. Yu, Photoluminescent colloidal nanohelices self-assembled from cdse magic-size clusters via nanoplatelets, *J. Phys. Chem. Lett.* **10**, 2794 (2019).

- [13] C. Bouet, B. Mahler, B. Nadal, B. Abecassis, M. D. Tessier, S. Ithurria, X. Xu, and B. Dubertret, Two-dimensional growth of CdSe nanocrystals, from nanoplatelets to nanosheets, *Chem. Mater.* **25**, 639 (2013).
- [14] S. Ithurria and B. Dubertret, Quasi 2D colloidal CdSe platelets with thicknesses controlled at the atomic level., *J. Am. Chem. Soc.* **130**, 16504 (2008); S. Ithurria, M. D. Tessier, B. Mahler, R. P. S. M. Lobo, B. Dubertret, and A. L. Efros, Colloidal nanoplatelets with two-dimensional electronic structure, *Nat. Mater.* **10**, 936 (2011).
- [15] D. A. Kurtina, A. V. Garshev, I. S. Vasil'eva, V. V. Shubin, A. M. Gaskov, and R. B. Vasiliev, Atomically thin population of colloidal CdSe nanoplatelets: Growth of rolled-up nanosheets and strong circular dichroism induced by ligand exchange, *Chem. Mater.* **31**, 9652 (2019).
- [16] X. Huang, V. K. Parashar, and M. A. M. Gijs, Spontaneous formation of CdSe photoluminescent nanotubes with visible-light photocatalytic performance, *ACS Cent. Sci.* **5**, 1017 (2019).
- [17] E. M. Hutter, E. Bladt, B. Goris, F. Pietra, J. C. van der Bok, M. P. Boneschanscher, C. de Mello Donegá, S. Bals, and D. Vanmaekelbergh, Conformal and atomic characterization of ultrathin cdse platelets with a helical shape, *Nano Lett.* **14**, 6257 (2014).
- [18] S. Singh, R. Tomar, S. ten Brinck, J. De Roo, P. Geiregat, J. C. Martins, I. Infante, and Z. Hens, Colloidal CdSe nanoplatelets, A model for surface chemistry/optoelectronic property relations in semiconductor nanocrystals, *J. Am. Chem. Soc.* **140**, 13292 (2018).
- [19] R. S. Koster, C. Fang, A. van Blaaderen, M. Dijkstra, and M. A. van Huis, Acetate ligands determine the crystal structure of cdse nanoplatelets – a density functional theory study, *Phys. Chem. Chem. Phys.* **18**, 22021 (2016).
- [20] J. Zhang, H. Zhang, W. Cao, Z. Pang, J. Li, Y. Shu, C. Zhu, X. Kong, L. Wang, and X. Peng, Identification of facet-dependent coordination structures of carboxylate ligands on CdSe nanocrystals, *J. Am. Chem. Soc.* **141**, 15675 (2019).
- [21] J. Owen, The coordination chemistry of nanocrystal surfaces, *Science* **347**, 615 (2015).
- [22] W. D. Kim, D.-E. Yoon, D. Kim, S. Koh, W. K. Bae, W.-S. Chae, and D. C. Lee, Stacking of colloidal CdSe nanoplatelets into twisted ribbon superstructures: Origin of twisting and its implication in optical properties, *J. Phys. Chem. C* **123**, 9445 (2019).
- [23] M. Zhang, D. Grossman, D. Danino, and E. Sharon, Shape and fluctuations of frustrated self-assembled nano ribbons, *Nat. Commun.* **10**, 3565 (2019).
- [24] S. Armon, E. Efrati, R. Kupferman, and E. Sharon, Geometry and mechanics in the opening of chiral seed pods, *Science* **333**, 1726 (2011).
- [25] A. I. Lebedev, Spontaneous strain in quasi-two-dimensional Janus CdSe nanoplatelets and its microscopic mechanisms, *J. Phys. Chem. C* **127**, 9911 (2023).
- [26] S. Armon, E. Efrati, R. Kupferman, and E. Sharon, Geometry and mechanics in the opening of chiral seed pods, *Science* **333**, 1726 (2011).
- [27] D. Grossman, E. Sharon, and H. Diamant, Elasticity and fluctuations of frustrated nanoribbons, *Phys. Rev. Lett.* **116**, 258105 (2016).
- [28] Y. Liu, Y. Li, S. Jeong, Y. Wang, J. Chen, and X. Ye, Colloidal Synthesis of Nanohelices via Bilayer Lattice Misfit, *J. Am. Chem. Soc.* [10.1021/jacs.0c05175](https://doi.org/10.1021/jacs.0c05175) (2020), tex.ids: liu\_colloidal\_2020-1 publisher: American Chemical Society.
- [29] S. Armon, H. Aharoni, M. Moshe, and E. Sharon, Shape selection in chiral ribbons: From seed pods to supramolecular assemblies, *Soft Matter* **10**, 2733 (2014).
- [30] A. P. Thompson, H. M. Aktulga, R. Berger, D. S. Bolintineanu, W. M. Brown, P. S. Crozier, P. J. in 't Veld, A. Kohlmeyer, S. G. Moore, T. D. Nguyen, R. Shan, M. J. Stevens, J. Tranchida, C. Trott, and S. J. Plimpton, LAMMPS - A flexible simulation tool for particle-based materials modeling at the atomic, meso, and continuum scales, *Comput. Phys. Commun.* **271**, 108171 (2022).
- [31] T. Kister, D. Monego, P. Mulvaney, A. Widmer-Cooper, and T. Kraus, Colloidal stability of apolar nanoparticles: The role of particle size and ligand shell structure, *ACS Nano* **12**, 5969 (2018).
- [32] E. Rabani, An interatomic pair potential for cadmium selenide, *J. Chem. Phys.* **116**, 258 (2002).
- [33] W. L. Jorgensen, D. S. Maxwell, and J. Tirado-Rives, Development and testing of the OPLS all-atom force field on conformational energetics and properties of organic liquids, *J. Am. Chem. Soc.* **118**, 11225 (1996).
- [34] W. L. Jorgensen and J. Tirado-Rives, Potential energy functions for atomic-level simulations of water and organic and biomolecular systems, *Proc. Natl. Acad. Sci.* **102**, 6665 (2005).
- [35] L. S. Dodda, J. Z. Vilseck, J. Tirado-Rives, and W. L. Jorgensen, 1.14\*CM1A-LBCC: Localized bond-charge corrected CM1A charges for condensed-phase simulations, *J. Phys. Chem. B* **121**, 3864 (2017).
- [36] L. S. Dodda, I. C. de Vaca, J. Tirado-Rives, and W. L. Jorgensen, LigParGen web server: an automatic OPLS-AA parameter generator for organic ligands, *Nucleic Acids Res.* **45**, W331 (2017).
- [37] L. Martínez, R. Andrade, E. G. Birgin, and J. M. Martínez, PACKMOL: A package for building initial configurations for molecular dynamics simulations, *J. Comput. Chem.* **30**, 2157 (2009).
- [38] M. L. Cohen and J. R. Chelikowsky, *Electronic structure and optical properties of semiconductors* (Springer-Verlag Berlin Heidelberg, 1988).
- [39] M. Grünwald, A. Zayak, J. B. Neaton, P. L. Geissler, and E. Rabani, Transferable pair potentials for CdS and ZnS crystals, *J. Chem. Phys.* **136**, 234111 (2012).
- [40] J. A. Zimmerman, E. B. WebbIII, J. J. Hoyt, R. E. Jones, P. A. Klein, and D. J. Bammann, Calculation of stress in atomistic simulation, *Model. Simul. Mater. Sci. Eng.* **12**, S319 (2004).
- [41] J. A. Zimmerman, R. E. Jones, and J. A. Templeton, A material frame approach for evaluating continuum variables in atomistic simulations, *J. Comput. Phys.* **229**, 2364 (2010).
- [42] J. A. Templeton, R. E. Jones, and G. J. Wagner, Application of a field-based method to spatially varying thermal transport problems in molecular dynamics, *Model. Simul. Mater. Sci. Eng.* **18**, 085007 (2010).
- [43] N. C. Admal and E. B. Tadmor, A unified interpretation of stress in molecular systems, *J. Elast.* **100**, 63 (2010).
- [44] N. C. Admal and E. B. Tadmor, Stress and heat flux for arbitrary multibody potentials: A unified framework, *J. Chem. Phys.* **134**, 184106 (2011).
- [45] J. Rigelesaiyin, A. Diaz, W. Li, L. Xiong, and Y. Chen, Asymmetry of the atomic-level stress tensor in homogeneous and inhomogeneous materials, *Proc. R. Soc. A*

- [474](#), [20180155](#) (2018).
- [46] M. Wang, Y. Huang, J. Li, L. Xu, and F. Zhu, Local stress field in wafer thinning simulations with phase space averaging, *Comput. Mater. Contin.* **68**, 743 (2021).
  - [47] H. Pottmann and T. Randrup, Rotational and helical surface approximation for reverse engineering, *Computing* **60**, 307 (1998).
  - [48] J. Andrews and C. H. Séquin, Generalized, basis-independent kinematic surface fitting, *Comput.-Aided Des.* **45**, 615 (2013).
  - [49] C. Shakarji, Least-squares fitting algorithms of the NIST algorithm testing system, *J. Res. Natl. Inst. Stand. Technol.* **103**, 633 (1998).
  - [50] G. Taubin, Estimation of planar curves, surfaces, and nonplanar space curves defined by implicit equations with applications to edge and range image segmentation, *IEEE Trans. Pattern Anal. Mach. Intell.* **13**, 1115 (1991).
  - [51] N. Chernov, *Circular and linear regression: Fitting circles and lines by least squares* (Chapman & Hall/CRC Press, Boca Raton, FL, 2010).
  - [52] J. Guo and J. Yang, An iterative procedure for robust circle fitting, *Commun. Stat. Simul. Comput.* **48**, 1872 (2019).
  - [53] D. Grossman, E. Sharon, and E. Katzav, Shape and fluctuations of positively curved ribbons, *Phys. Rev. E* **98**, 022502 (2018).

**SUPPLEMENTARY MATERIAL**

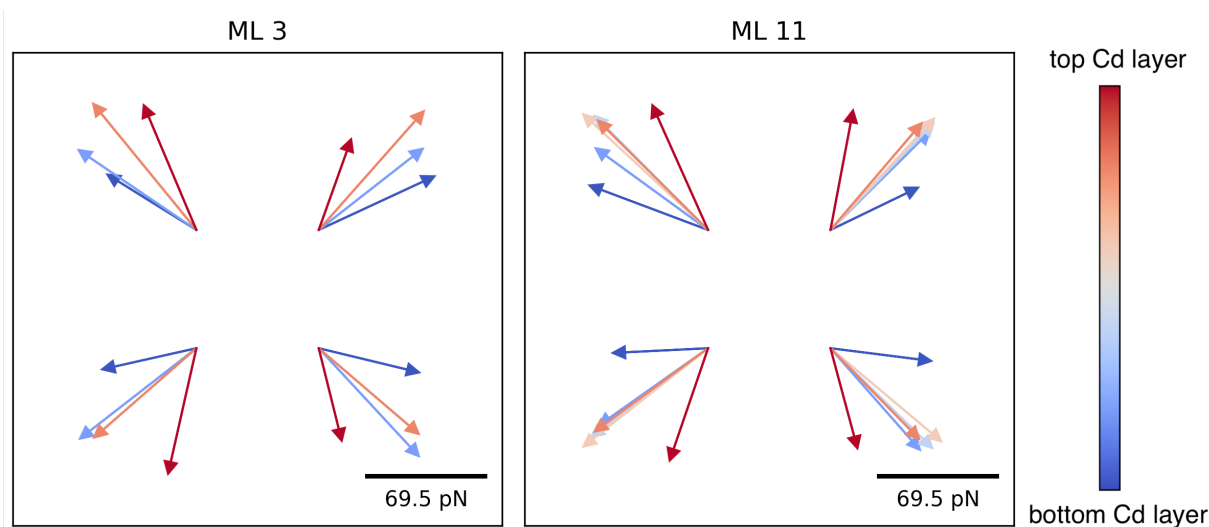


FIG. S1. In-plane forces, averaged over each quadrant, for the Cd layers (which correspond to the (001) planes) of a 3 ML (left) and a 11 ML (right) 10 nm by 10 nm NPL with  $\alpha = 0$ . The thickness of the 3ML NPL is 1.1 nm, and that of the 11 ML NPL is 3.5 nm. The scale bar on the right of the plots provides a measure of the magnitude of the forces, while the arrows show their direction. Colors represent different Cd layers, going from the nanocrystal's bottom (dark blue) to the top (dark red) surface.

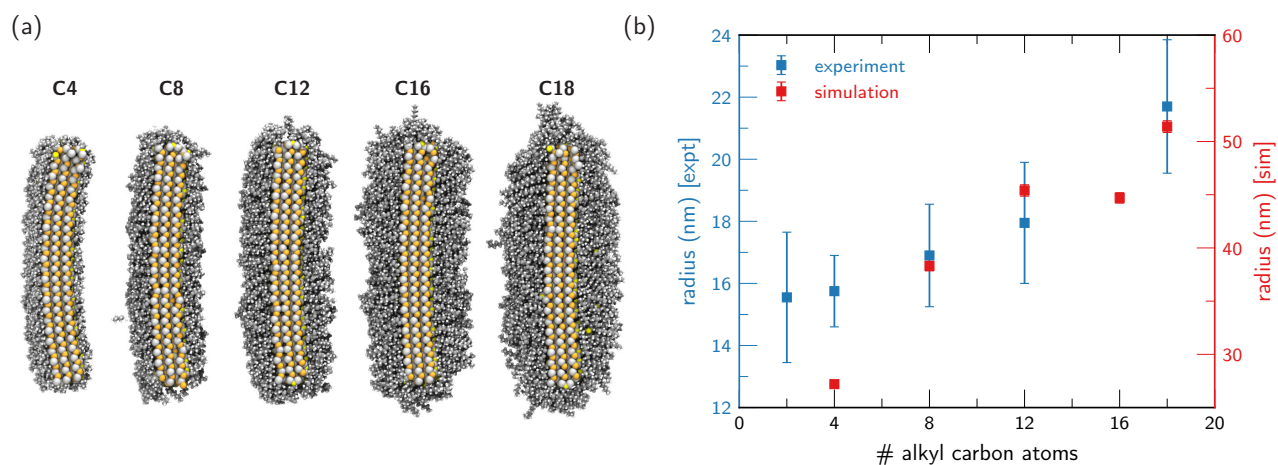


FIG. S2. Effect of ligand chain length on the curvature. (a) Snapshots of simulated CdSe NPL of lateral dimensions 10 nm  $\times$  10 nm and thickness 1.7 nm (5 ML) at  $\alpha = 0$  coated with linear alkyl thiol ligands with 4-18 carbon atoms in length. (b) The radius of curvature as a function of carbon number from MD simulations and experiments by [5]. Error bars indicate 95% confidence intervals. The numerical difference between the two data sets is partially due to the simulations being run at lower temperatures than the experiments (100 K vs 300 K), which was done to obtain more reliable estimates for the radius of curvature.

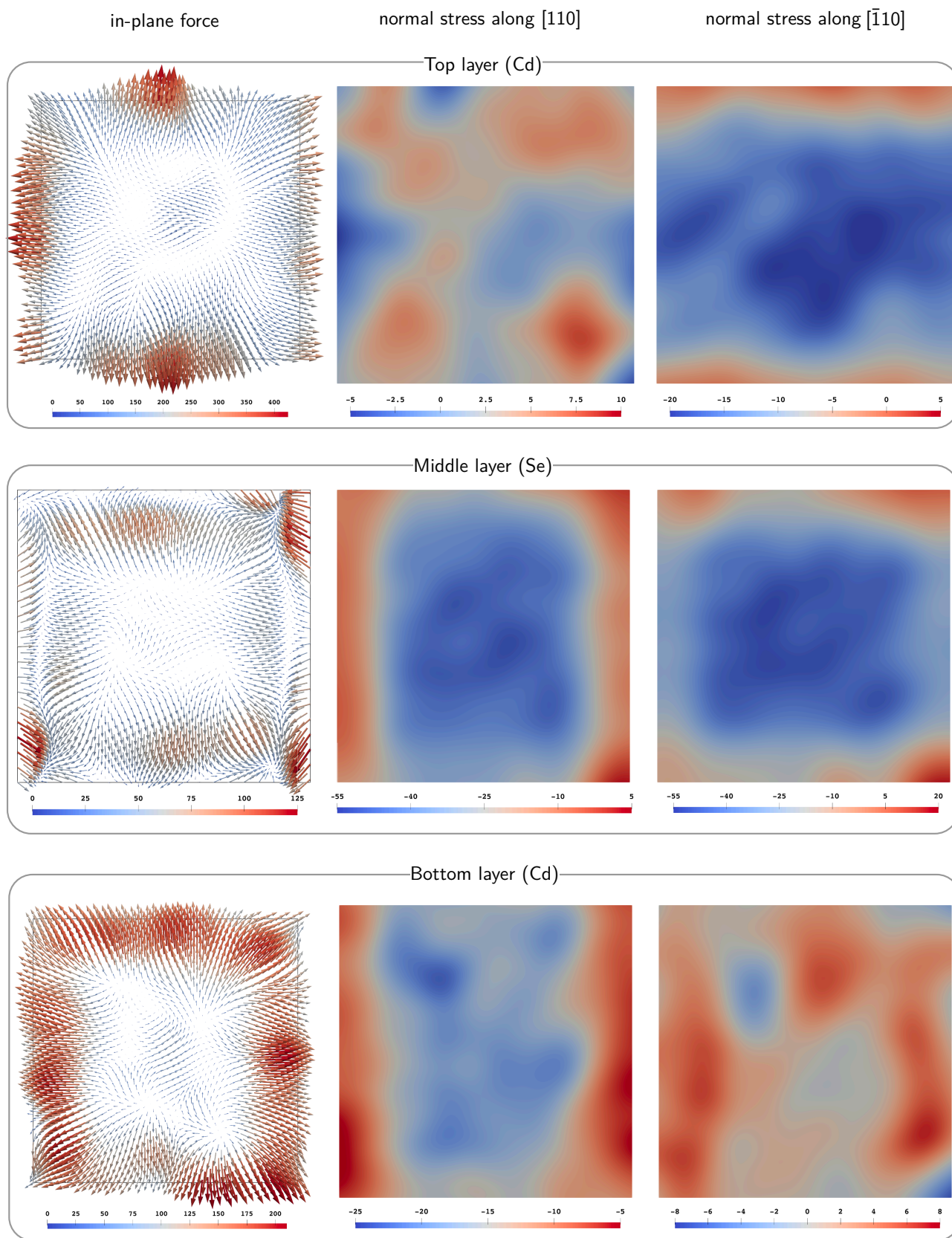


FIG. S3. In-plane forces on each atom (in pN) and normal stresses (in GPa) at the top, middle, and bottom layers of a 3 ML (thickness 1.1 nm) 10 nm × 10 nm CdSe NPL coated with acetate ligands at 100 K, obtained from time-averaging from 100 fs to 300 fs after the onset of deformation. In the case of the force plots, the color coding indicates the magnitude of the in-plane forces.

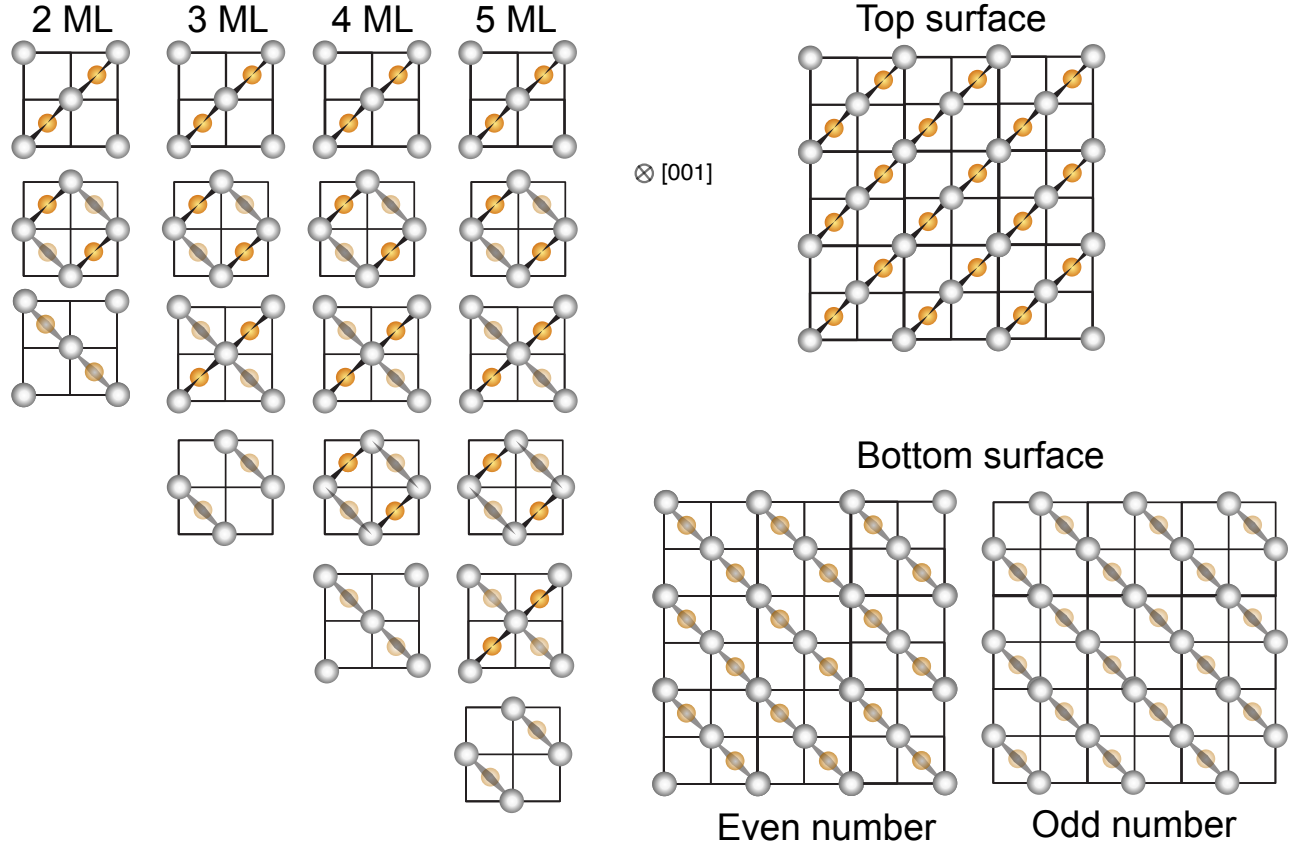


FIG. S4. Crystallographic The structure of CdSe zinc-blende NPL depends on the number of monolayers viewed from the [001] direction. The atomic configurations for 2 to 5 monolayers are displayed on the left. On the right, the top and bottom surfaces show perpendicular Cd-Se bonding patterns for an even and an odd number of monolayers.

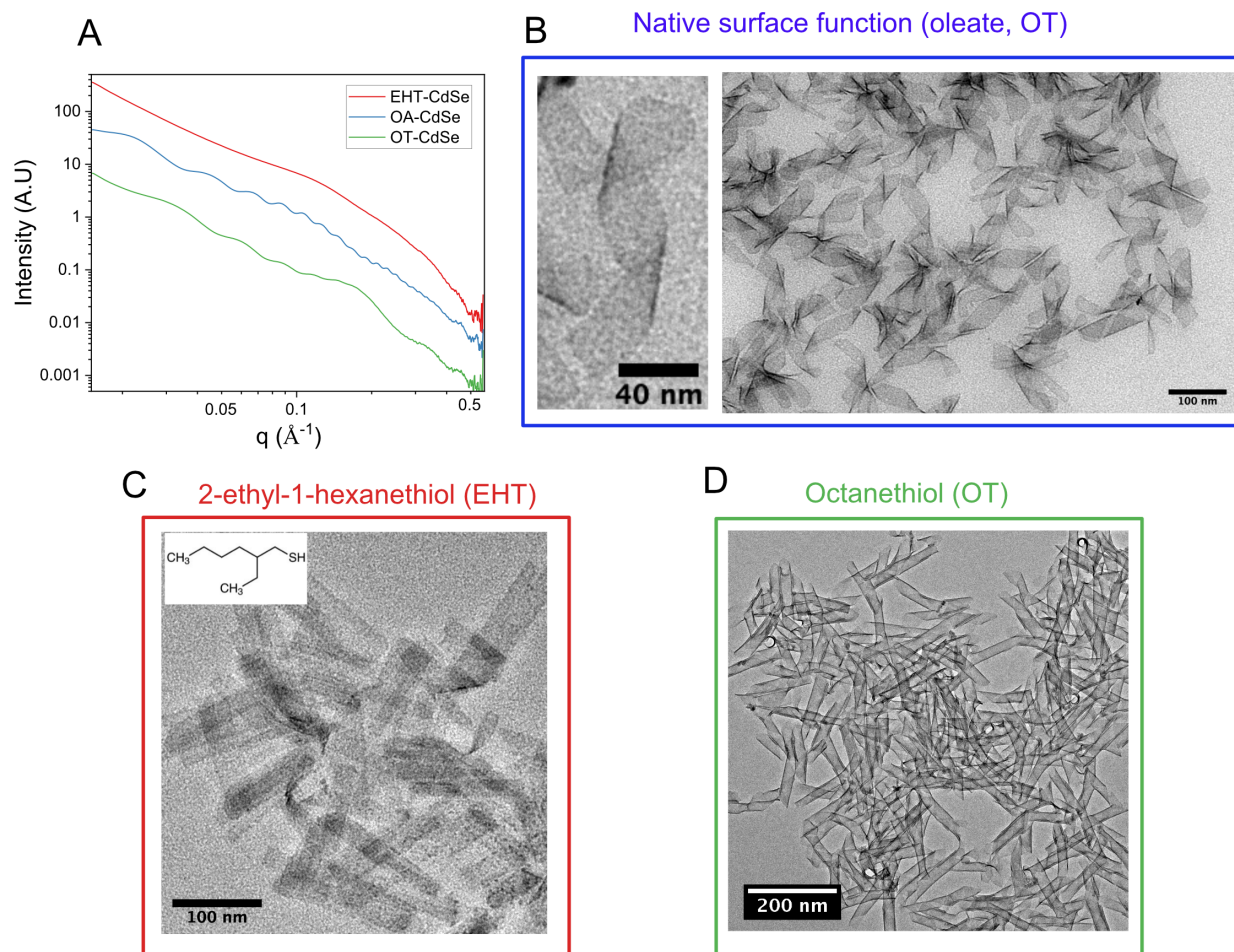


FIG. S5. Effect of ligand chain structure on the curvature. A) SAXS patterns of CdSe NPL dispersion with different surface functions: oleate (native surface function), octanethiol and 2-ethyl-1-hexanethiol (EHT). The  $q^{-2}$  slope indicates a flat NPL geometry. The oscillations in the oleate and octanethiol patterns indicate a curved surface. B) TEM images of CdSe NPL showing a helical ribbon geometry. C) TEM image of the same NPL after ligand exchange with (EHT) showing the unfolding of the helical ribbon into flat NPL D) TEM image of the same NPL after ligand exchange with octanethiol showing a curved geometry.